Supplementary Material

A precision medicine approach to the rescue of function in malignant calmodulinopathic long QT syndrome

Limpitikul *et al*, Circulation Research

Table of Contents

1. Additional Data

1.1 Characterization of the iPSC clones

The iPSC clones generated in this study were derived from a skin biopsy from a patient harboring a p.D130G-CaM mutation residing in the *CALM2* gene[1]. In order to ensure the quality of the generated iPSCs, the karyotype and pluripotency of the cells were fully characterized and validated (Online Figure I).

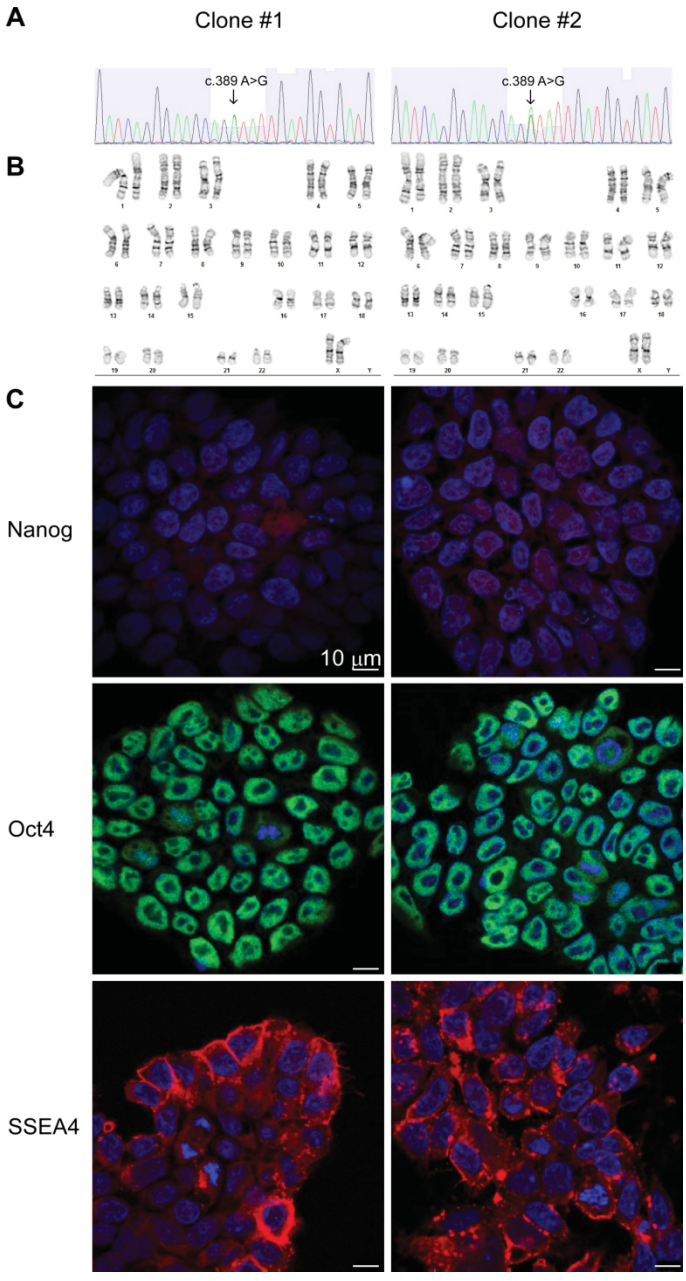

Online Figure I. Assessment of karyotype and pluripotency markers for the iPSC clones. A, Sanger sequencing of *CALM2* genomic DNA confirms c.389 A>G. **B**, Karyotyping results of both iPSC clones revealed normal size, shape, and number of chromosomes. Karyotyping was commercially performed by WiCell Cytogenetics. **C**, Immunohistochemistry demonstrated the presence of pluripotency markers: Nanog (red), Oct4 (green), and SSEA4 (red). Nuclei are counter-stained with DAPI (blue).

1.2 iPSC$_{D130G\text{-}CaM}$ clones are capable of differentiating into three germ layers

An important feature of iPSC lines is pluripotency; that is, the ability to differentiate into all three germ layers, endoderm, mesoderm, and ectoderm. We have confirmed the pluripotency of iPSC$_{D130G\text{-}CaM}$ clones both *in vitro* and *in vivo*. First, embryoid bodies were generated *in vitro* and markers of three germ layers were labeled by immunohistochemistry (Online Figure II(A)). Next, the ability of iPSC clones to form teratomas *in vivo* was assessed by injection of iPSCs into immunodeficient mice (Online Figure II(B)). The haematoxyline and eosin staining of the harvested teratomas revealed tissues from endodermal, mesodermal and ectodermal origins.

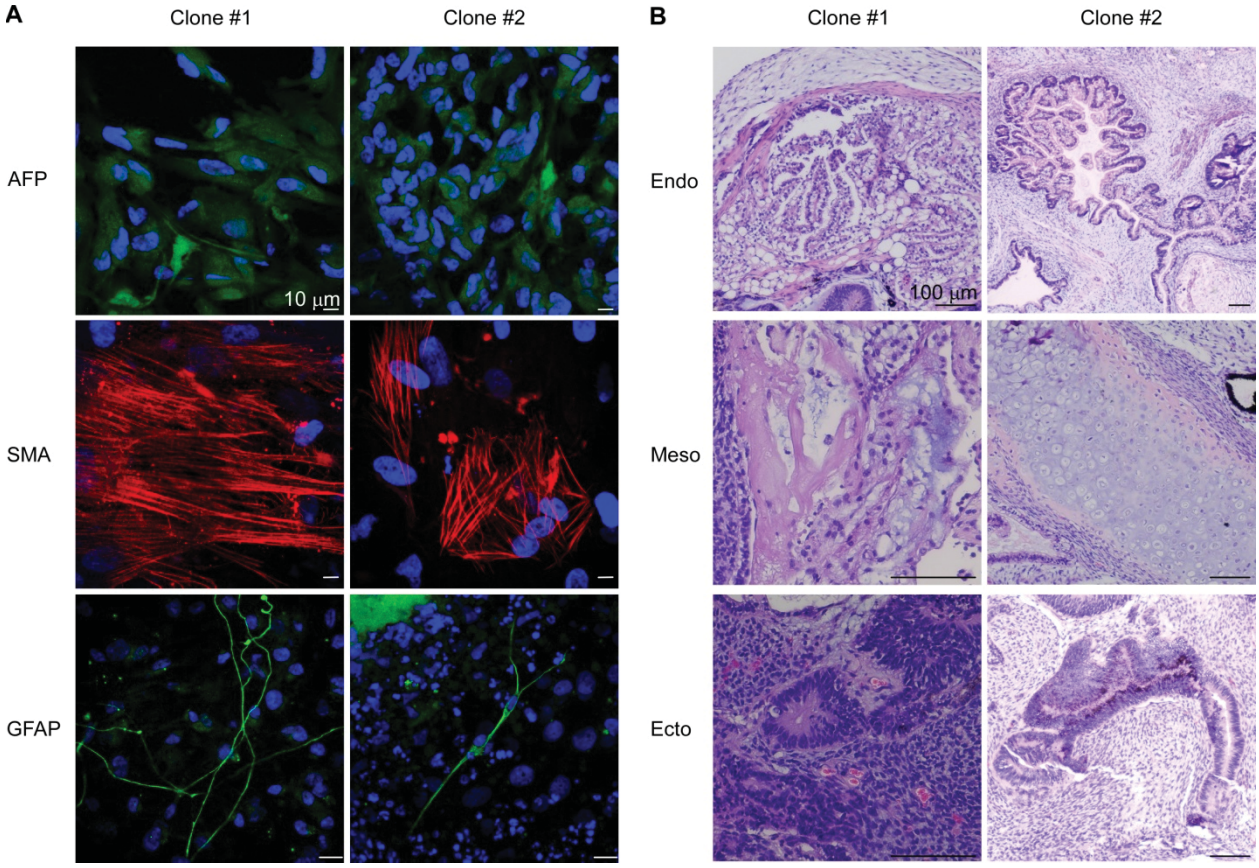

Online Figure II. Ability of iPSCs$_{D130G\text{-}CaM}$ to differentiate into all germ layers. A, Immunostaining of differentiated embryoid bodies for the endoderm-specific α-fetoprotein (AFP, green), the mesoderm-specific smooth muscle actin (SMA, red), and the ectoderm-specific glial fibrillary acid protein (GFAP, green). Cells are counter-stained with DAPI for visualization of the nuclei (blue). **B**, Five-to-eight-week-old teratomas harvested from mice injected with undifferentiated iPSCs$_{D130G\text{-}CaM}$. Tissue sections were stained with haematoxyline and eosin. All three germ layers, including gut-like structures (Endo: endoderm), immature bone and cartilage (Meso: mesoderm), and immature neural tube and neuroectoderm (Ecto: ectoderm), are identifiable in teratomas generated from both iPSCs$_{D130G\text{-}CaM}$ clones.

1.3 Expression of genetically encoded sensors

Expression of the voltage sensor ASAP1 and the calcium sensor GCaMP6f was assesed by flow cytometry 7-10 days aftter transduction (Online Figure III). A large fraction of cells expressed the ASAP sensor, while a smaller fraction expressed the GCaMP6f sensor. The expression of GCaMP6f was kept low so as to reduce the potential effect of the sensor on resting the Ca^{2+} concentration.

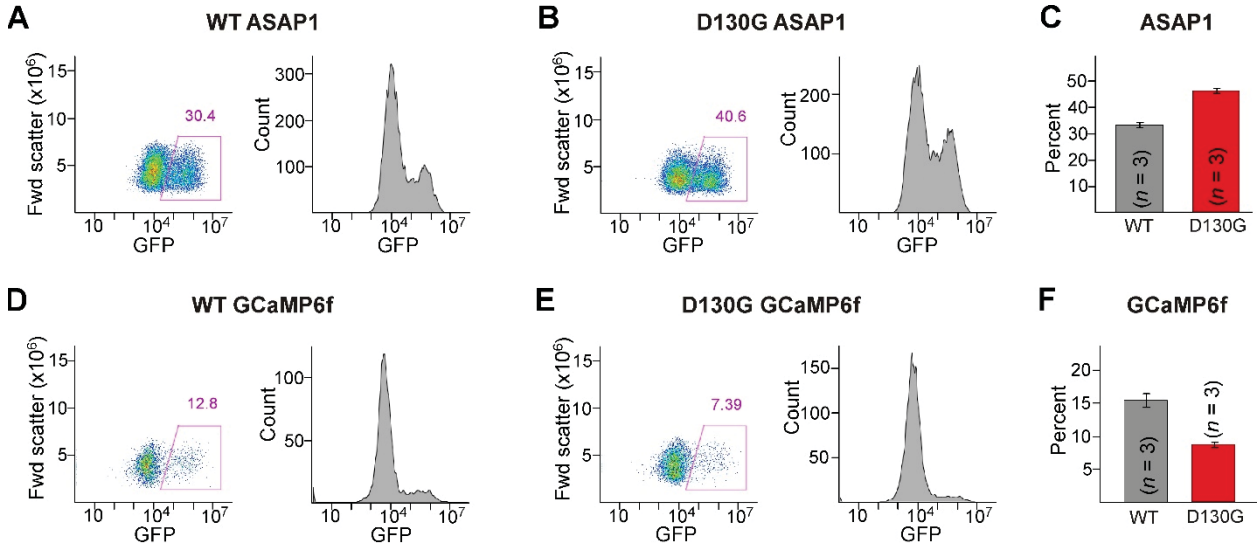

Online Figure III. Quantification of sensor expression. A-B, Exemplar scatter and histogram plots of $iPSC_{WT}$-CMs and $iPSC_{D130G\text{-}CaM}$-CMs expressing ASAP1. **C,** Population data of ASAP1 expression level gauged by percentage of fluorescent cells in both iPSC-CM clones. **D-E,** Exemplar scatter and histogram plots of $iPSC_{WT}$-CMs and $iPSC_{D130G\text{-}CaM}$-CMs expressing GCaMP6f. **F,** Population data of GCaMP6f expression level gauged by % of fluorescent cells in both iPSC-CM clones indicating the percentage of $iPSC_{WT}$-CMs which express GCaMP6f.

1.4 QPCR analysis of iPSC-CM mRNA levels

In this study, we utilized iPSC-CMs with different individual genetic backgrounds for control (WT) and calmodulinopathy cells. In order to ensure that these cells are an appropriate control, we examined the RNA profile of the $iPSC_{WT}$-CMs as compared to the $iPSC_{D130G\text{-}CaM}$-CMs, focusing on those proteins which might contribute to alterations in QT interval or calcium handling (Online Figure IV). Very little difference was found between the two iPSC-CM lines, with only a small elevation in KCNQ1 (Online Figure IV(E)) and RYR2 (Online Figure IV(H)) detected. Importantly, this difference cannot account for the LQT phenotype of these cells. In fact, increased levels of KCNQ1 would tend to decrease the QT interval. Moreover, treatment of the $iPSC_{D130G\text{-}CaM}$-CMs did not alter the mRNA level for any protein tested, with the exception of the targeted *CALM2* gene, indicating specificity of the treatment.

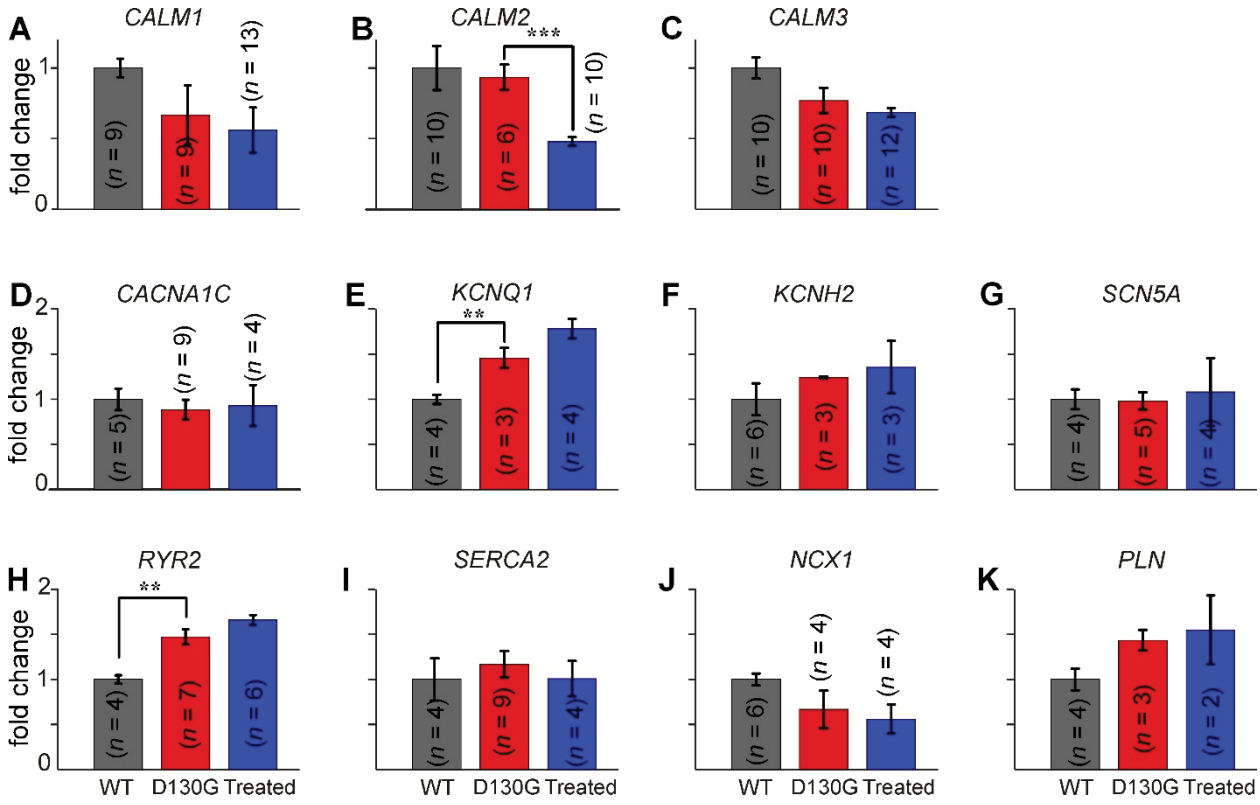

Online Figure IV. Analysis of the genetic background of WT, D130G and D130G treated cells. A, QPCR results indicating mRNA levels of multiple relevant proteins from $iPSC_{WT}$-CMs (gray), $iPSC_{D130G\text{-}CaM}$-CMs (red) and treated $iPSC_{WT}$-CMs (Blue) (** $p<0.01$, *** $P<0.001$). Error bars indicate ± SEM. n indicates biological replicates.

1.5 Total calmodulin protein levels in iPSC-CMs

The total calmodulin protein levels in $iPSC_{WT}$-CMs and $IPSC_{D130G\text{-}CaM}$-CMs was assessed using western blot analysis (Online Figure V). No difference was seen between these two cell lines; however a small but statistically significant decrease in calmodulin protein was seen following treatment with CRISPRi, consistent with a decrease in *CALM2* expression.

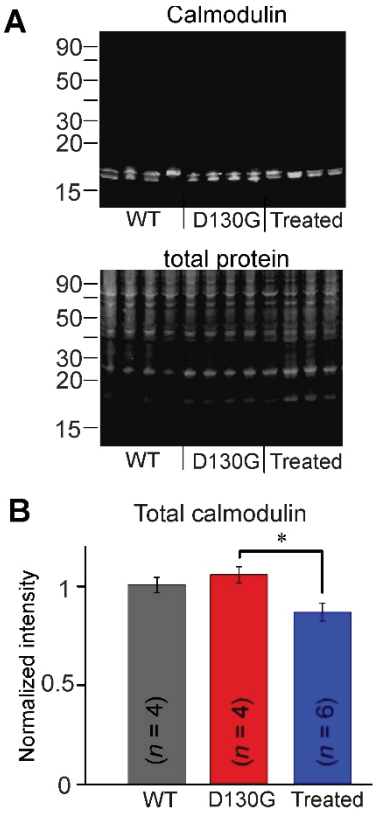

Online Figure V. Assessment of calmodulin protein expression. A, Western blot of $iPSC_{WT}$-CMs, $iPSC_{D130G\text{-}CaM}$-CMs and treated $iPSC_{D130G\text{-}CaM}$-CMs probed with anit-calmodulin. Samples were normalized to total protein as determined with a Coomassie stain (inverted intensity image shown at the bottom). **B**, Normalized intensity of the calmodulin protein bands. No difference in calmodulin levels were detected between $iPSC_{WT}$-CMs (gray) and $iPSC_{D130G\text{-}CaM}$-CMs (red), however treatment produced a small decrease in calmodulin protein (blue). * $p<0.05$. Error bars indicate ± SEM.

1.6 The AP phenotype is stable at multiple time points

In the main text we demonstrated APD prolongation at multiple cycle lengths in iPSC$_{D130G\text{-}CaM}$-CMs 30 days post-differentiation (Figure 1D-L). The equivalent data was obtained 45 and 60 days post-differentiation (Online Figure VI) on the same population of monolayers in Figure 1**,** demonstrating that the phenotype of the iPSC$_{D130G\text{-}CaM}$-CMs is stable over time. Summary data for a cycle length of 2 seconds is displayed in main text Figures 1F, I, L.

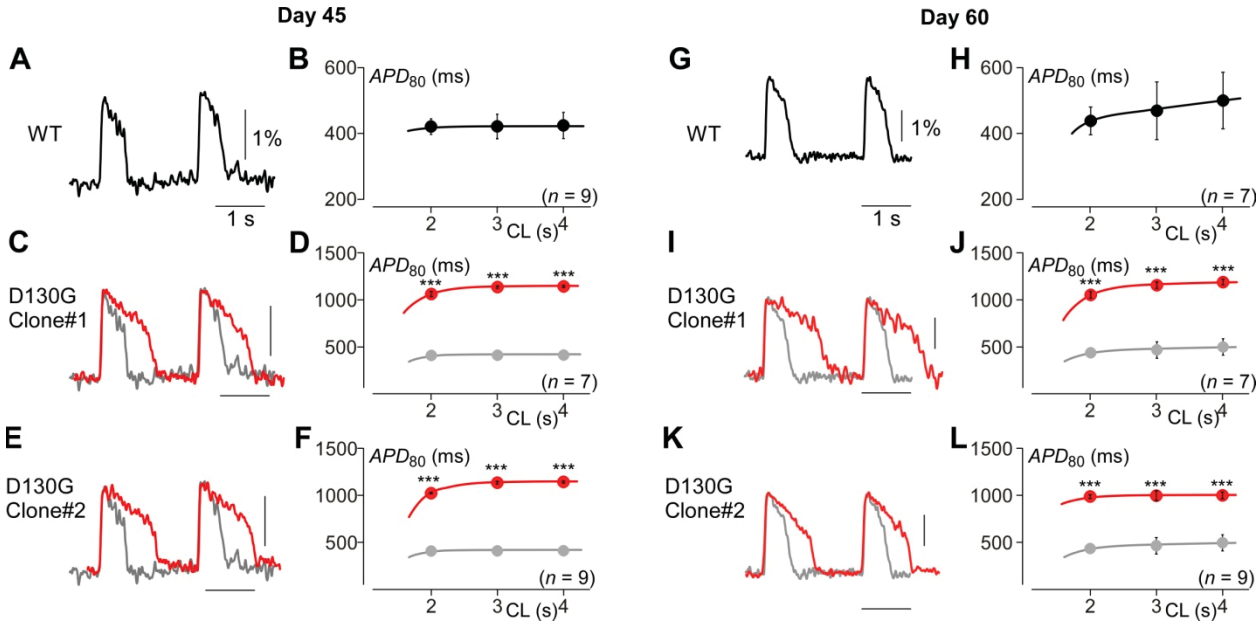

Online Figure VI. Stability of iPSC-CM APs across multiple time points. A, Exemplar APs from iPSC$_{WT}$-CMs paced at 0.5 Hz, recorded via fluorescence imaging using ASAP1 45 days post-differentiation. Scale bar indicates percent change in fluorescence. **B**, Population data for average APDs at various cycle lengths (CL) for 45-day-old iPSC$_{WT}$-CMs (n=9). Each biological replicate (n) is an average value of 2 technical replicates/measurements for all data in this figure. Error bars indicate ± SEM throughout. **C**, Exemplar APs from 45-day-old iPSC$_{D130G\text{-}CaM}$-CMs (red). WT reproduced in gray. **D**, Average APD data for iPSC$_{D130G\text{-}CaM}$-CMs (red, n=7) across multiple pacing frequencies. WT reproduced in gray (*** $p<0.001$ compared to WT and corrected for unequal variance, both population normally distributed). **E-F**, Alternate D130G clone demonstrating the same result as **C, D** (n=9, *** $p<0.001$ compared to WT and corrected for unequal variance, both population normally distributed). **G-L**, Equivalent results were observed for iPSC$_{D130G\text{-}CaM}$-CMs 60 days post-differentiation. Format as in **A-F**. (n=7, 7, and 7 for WT, D130G clone#1, and D130G clone#2, respectively; (*** $p<0.001$ compared to WT and corrected for unequal variance, both populations normally distributed)

1.7 Disruption of Ca^{2+} cycling across multiple time points

In the main text we demonstrated significant disruption of Ca^{2+} cycling, with CaT amplitudes several fold larger in $iPSC_{D130G\text{-}CaM}$-CMs as compared to their WT counterparts (Figures 2A-F). The data was collected 30 days post-differentiation, however comparable results could also be obtained 45 and 60 days post-differentiation from the same population of monolayers in Figure 2 (Online Figure VII), indicating a stable phenotype of the D130G harboring monolayers.

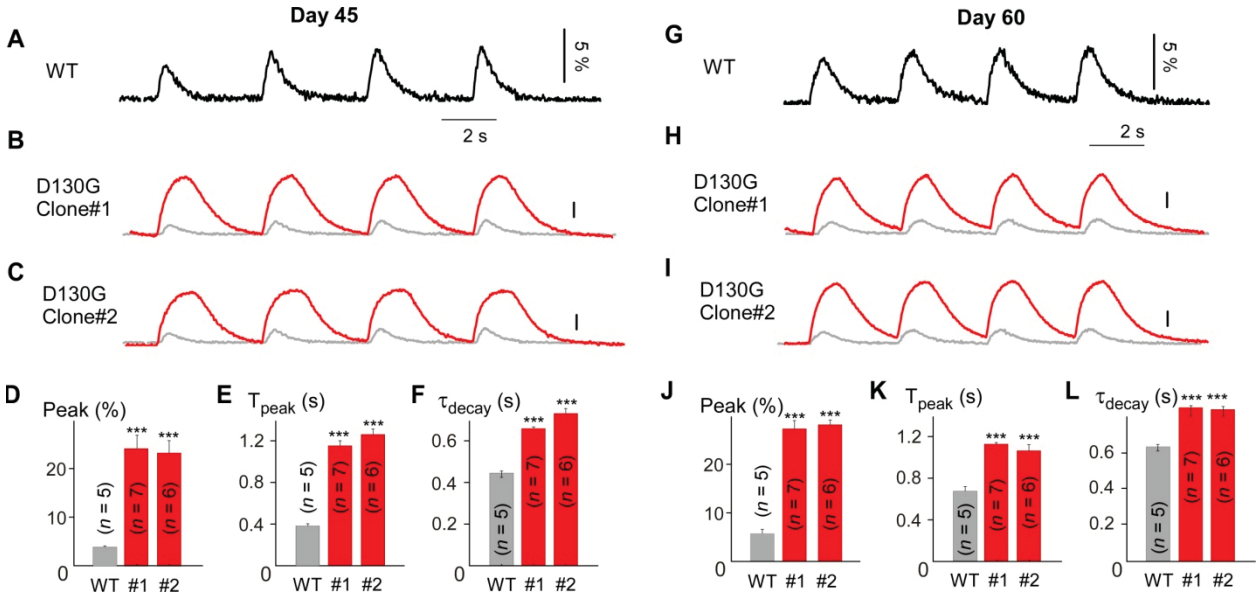

Online Figure VII. Stability of iPSC-CM CaTs across multiple time points. A, Exemplar CaTs recorded from 45-day-old $iPSC_{WT}$-CMs (WT) using GCaMP6f. Scale bar indicates percent change in fluorescence. **B**, Exemplar CaTs recorded from $iPSC_{D130G\text{-}CaM}$-CMs (red) 45 days post-differentiation, as compared to WT (gray). **C**, Exemplar CaTs from an alternate D130G clone 45 days post-differentiation. **D-F**, Population data demonstrating larger amplitude and slower kinetics for both $iPSC_{D130G\text{-}CaM}$-CMs clones compared to WT after 45 days in culture (red) (Peak, average peak fluorescence change; Tpeak, average time to peak; τ_{decay}, average decay time constant; n=5, 7, and 6 for WT, D130G clone #1, and D130G clone #2, respectively; *** $p<0.001$ compared to WT and corrected for unequal variance, both population normally distributed). Each biological replicate (n) is an average value of 2 technical replicates/measurements for all data in this figure. **G-L**, Equivalent results were seen for $iPSC_{D130G\text{-}CaM}$-CMs 60 days post-differentiation. Format as in **A-F**. (n=5, 7, and 6 for WT, D130G clone #1, and D130G clone #2, respectively; *** $p<0.001$ compared to WT and corrected for unequal variance, both population normally distributed)

1.8 SR content effects in iPSC$_{D130G\text{-}CaM}$-CMs

Given the large effects of the calmodulinopathy mutation on CaTs, we examined the SR content of these cells via application of 5 mM caffeine. While the SR content did appear somewhat enhanced in the iPSC$_{D130G\text{-}CaM}$-CMs as compared to their WT counterparts (Online Figure VIII), this increase did not reach a level of statistical significance. This lack of a significant effect may be representative of the relatively immature nature of the iPSC-CMs[6, 7].

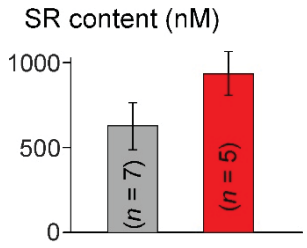

Online Figure VIII. SR content of iPSC$_{D130G\text{-}CaM}$-CMs. No statistical difference was seen in the SR content of iPSC$_{D130G\text{-}CaM}$-CMs (red) as compared to iPSC$_{WT}$-CMs (gray). SR content was assessed by application of caffeine while imaging the Ca^{2+} sensitive dye Indo-1. Error bars indicate SEM across coverslips (biological replicates).

1.9 Disruption of Ca^{2+}/CaM-dependent inactivation (CDI) of LTCCs at the older differentiation age

In the main text we demonstrated significant disruption of CDI of LTCCs in $iPSC_{D130G\text{-}CaM}$-CMs as compared to their WT counterparts (Figure 3). The data was collected 30 days post-differentiation, however comparable results could also be obtained 60 days post-differentiation (Online Figure IX), indicating a stable phenotype of the D130G harboring monolayers.

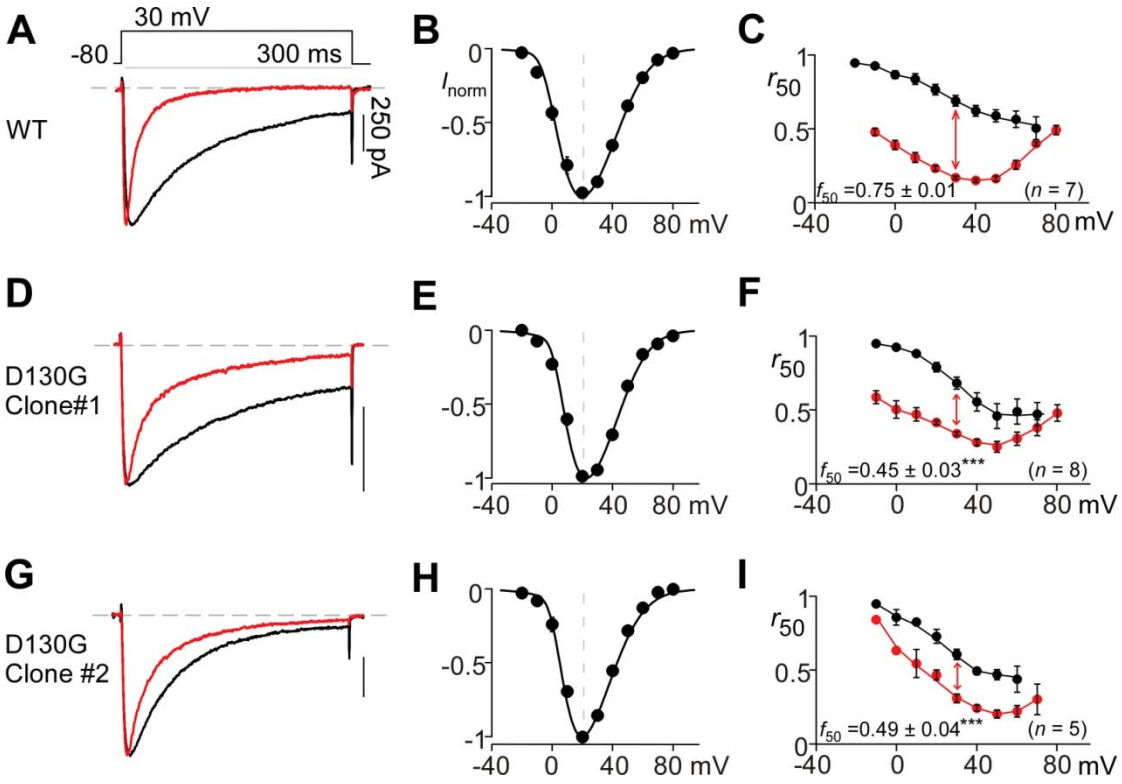

Online Figure IX. Stability of iPSC-CM LTCC CDI at later time point in culture. A, Exemplar whole-cell current recordings in Ca^{2+} (red) and Ba^{2+} (black) for $iPSC_{WT}$-CMs 60 days post-differentiation. Ba^{2+} current is normalized to Ca^{2+} peak, scale bar corresponds to Ca^{2+}. **B**, Average normalized current and voltage relationship for $iPSC_{WT}$-CMs (n=7, no technical replicate). Error bars indicate ± SEM throughout. **C**, Population data for Ca^{2+} (red) and Ba^{2+} (black) for $iPSC_{WT}$-CMs (n=7, no technical replicate), where r_{50} quantifies the extent of current inactivation across voltages. Red arrow depicts extent of CDI (f_{50}) at 30-mV test potential here and throughout. **D**, Exemplar whole-cell current recordings in Ca^{2+} (red) and Ba^{2+} (black) for $iPSC_{D130G\text{-}CaM}$-CMs 60 days post-differentiation. Ba^{2+} current is normalized to Ca^{2+} peak, scale bar corresponds to Ca^{2+}. **E**, There is no significant shift in the current voltage relationship for $iPSC_{D130G\text{-}CaM}$-CMs ($p>0.05$) as compared to WT (**B**). **F**, Population data demonstrates a significant decrease in CDI for the $iPSC_{D130G\text{-}CaM}$-CMs (n=8, ***$p<0.001$ compared to WT, corrected for unequal variance). **G-I**, Alternate D130G clone at 60 days post-differentiation demonstrating the same result as **D-F** (n=5, ***$p<0.001$ compared to WT, corrected for unequal variance).

1.10 A pharmacological study of LQT effects in iPSC-CMs

Of the various forms of LQT, only three correspond to disruptions in membrane channels known to associate with calmodulin: LQT1 (loss of function mutations in KCNQ1), LQT3(gain-of-function mutations in SCN5A), and LQT8 (gain-of-function mutations in CACNA1C). We therefore utilized a pharmacological approach to demonstrate that each of these LQT phenotypes could be recapitulated within our $iPSC_{WT}$-CMs. Application of the LTCC antagonist BayK 8644 more than doubled the APD_{80} of $iPSC_{WT}$-CMs (Online Figure X(A)). Such a profound effect on APD is matched in the clinical setting only by LQT8 (Timothy Syndrome) and LQT15 (calmodulinopathies) (Online Figure X(C)), supporting the supposition that the LQT seen in calmodulinopathy patients is due, in large part, to disruption of LTCC channels. Application of maximal doses of I_{KS} blocker, chromanol 293B, or the $Na_V1.5$ channel agonist, ATX II, produced moderate APD prolongation (Online Figure X(A,B)), corresponding to the clinical phenotype of LQT1 and 3 patients (Online Figure X(C)).

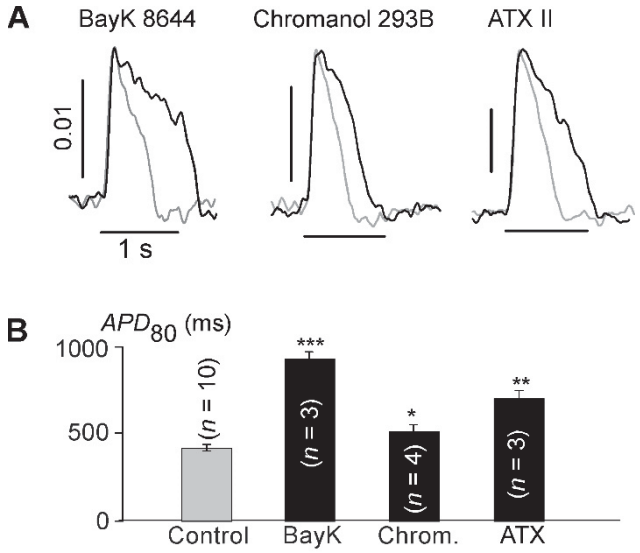

C

Type	Gene	QTc
LQT1	KCNQ1	400-600
LQT3	SCN5A	400-600
LQT8	CACNA1C	480-730
LQT15	CALM2	550-740

Online Figure X. Pharmacological study of APD prolongation in $iPSC_{WT}$-CMs. A, Exemplar AP recordings of $iPSC_{WT}$-CMs (gray) in the presence of 10 μmol/L BayK 8644 (left, black), 10μmol/L chromanol 293B (middle, black) or 0.5 μmol/L ATX II (right, black). **B**, Average APD_{80} values measured for each drug. Error bars indicate ± SEM throughout. **C**, Comparison of reported QT intervals corresponding to LQT syndromes associated with channels known to interact with CaM.

1.11 A modeling study of calmodulinopathy CDI deficits

We have demonstrated a reduction in LTCC CDI underlying the LQTS phenotype of $iPSC_{D130G\text{-}CaM}$-CMs (Figure 3). However, it is not possible to rule out the contribution of other CaM targets to the overall phenotype. We therefore considered whether a CDI specific effect of CaM_{D130G} on the LTCC would be sufficient to produce a calmodulinopathy phenotype. To this end, we utilized a validated and publically available model of an adult mammalian ventricular myocyte (the Luo-Rudy model: LRd)[1-4]. With this *in silico* method, we were able to selectively adjust the CDI of the LTCC channel to match the CDI data obtained for this mutation (Figure 3)[8]. In addition, this model provides insight into calmodulinopathy associated arrhythmias in an adult myocyte featuring intact EC coupling[2, 6]. In consideration of the variable expression of mutant CaM expected among calmodulinopathy patients, the model was run with variable fractions of LTCC channels harboring CaM_{D130G}. The result was APD prolongation which was dependent on expression levels of CaM_{D130G} in a non-linear manner (Online Figure XI). At low levels of CaM_{D130G} expression, the APD increased monotonically, however a threshold for severe electrical instability was reached near a ratio of one in six LTCCs harboring a CaM_{D130G} versus CaM_{WT}. Importantly, this corresponds to the expected expression levels of mutant CaM among calmodulinopathy patients, where the cardiac expression of a single *CALM* allele was determined to be 0.17 ± 0.02 (*CALM1*), 0.12 ± 0.01 (*CALM2*), and 0.21 ± 0.03 (*CALM3*) based on the average expression levels from five different RNAseq databases[5]. Thus calmodulinopathy patients appear to lie directly in the vicinity of the threshold for APD instability, making them highly susceptible to cardiac arrhythmia.

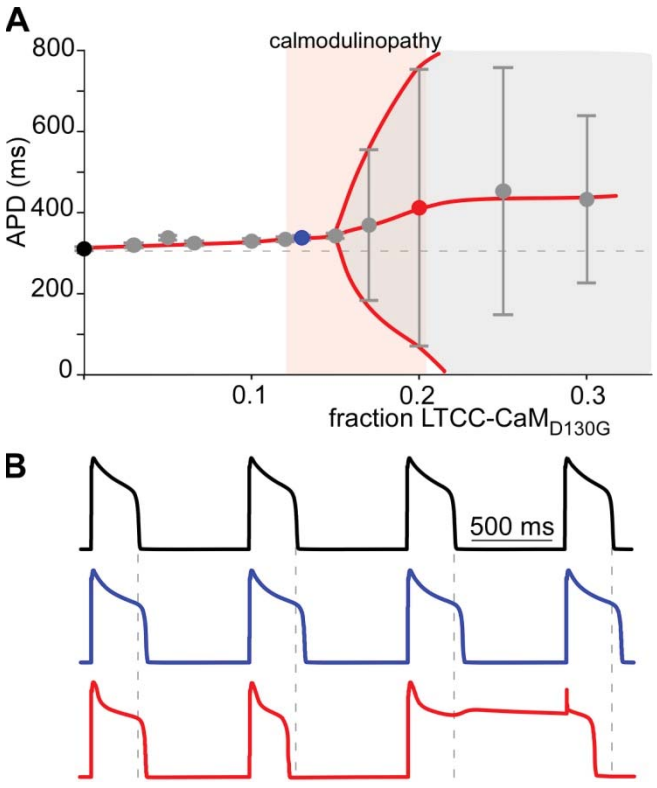

Online Figure XI. Modeling of a non-linear dose dependence of APDs on mutant CaM expression. A, Average APDs determined from an adult mammalian ventricular myocyte model[1-4], plotted as a function of the fraction of LTCCs harboring CaM_{D130G} (relative to the total number of LTCCs). Data is plotted ±SEM. The gray area indicates electrical instability in the modeled action potentials. The rose shading depicts the range of physiologically relevant expression levels for mutant CaM based on RNAseq databases for normal human gene expression levels[5]. **B**, Exemplar action potentials simulated at 1-Hz pacing corresponding to the colored points in **A**. Black: no CaM_{D130G}; Blue: 0.12 CaM_{D130G}; Red: 0.2 CaM_{D130G}.

1.12 GRNA screening

Over twenty different gRNAs targeted to *CALM1*, *CALM2* and *CALM3* were screened (Online Figure XII). Design 21 (Kg116) was chosen for treatment of the *CALM2* iPSC$_{D130G\text{-}CaM}$-CMs (Figure 4) as this design demonstrated significant efficacy against *CALM2*, and no appreciable effect against *CALM1* or *CALM3*. Similarly, design 2 was used for selective efficacy against *CALM1* (Figure 5B), and design 8 was utilized for *CALM3* (Figure 5C).

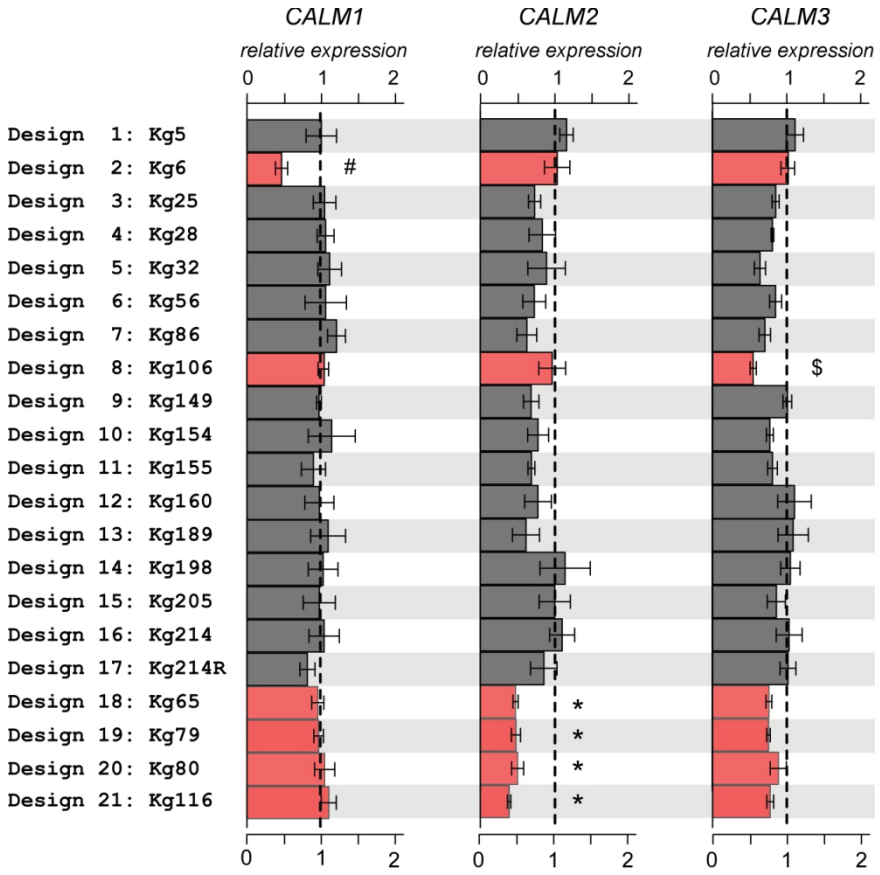

Online Figure XII. GRNA screening. QPCR results indicating mRNA levels of *CALM1-3* in HEK293 cells after CRISPRi treatment using various candidate gRNA sequences. The dashed line at 1 indicates control cells treated with scrambled gRNA. Designs 18-21 (rose) caused a significant decrease in *CALM2* mRNA (n=3, * $p<0.05$ compared to control) without altering *CALM1* or *CALM3*, while design 2 selectively decreased *CALM1* (n=4, # $p<0.05$ compared to control) and design 8 selectively decreased *CALM3* (n=6, $ $p<0.05$ compared to control). Each biological replicate (n) is an average value of 3 technical replicates/measurements for all data in this figure.

Online Table I: Sequence of candidate gRNAs

gRNA design	Sequence
Target *CALM1*:	
Kg5	GGCCGTTACTCGTAGTCAGG
Kg6	GGCCGCCTGACTACGAGTAA
Kg160	GCTACCATGGTGCGAGCGAA
Target *CALM2*:	
Kg25	GACGTACCTTATCAAACACA
Kg28	GCCATCATTGTCAGAAATTC
Kg56	GGAGCTTCACTCTCTTGCCC
Kg65	GGACAATGACAGTAAGATAA
Kg79	GATCGCTGAGCTGCCGGCGC
Kg80	GTCGCTGAGCTGCCGGCGCT
Kg86	GTTGGAGTTTATCTAGTGAA
Kg116	GCTACTTTCCCTTTCTAGTA
Kg149	GCGCCTCCCTTACACCTTCA
Kg154	GCCCTTACACCTTCAAGGAG
Kg155	GACCACTCCTTGAAGGTGTA
Kg189	GGATGGCGCGAAAGAGGCCA
Kg198	GTTTCTACCCGCGTTGTCGG
Kg205	GCAACCGTCGCCGGCATCCC
Kg214	GCCGGCGACGGTTGTGTCGC
Kg214R	GCCTGCGACACAACCGTCGC
Target *CALM3*:	
Kg32	GGTCCGGAGCACGGGGATCA
Kg106	GCTCTGAGGCGGGCTTAACG
Kg198	GTTTCTACCCGCGTTGTCGG

Online Table II: reported action potential duration in other control iPSC-CM lines

APD_{90} (ms)	Reference
477	Du *et al*., 2015[9]
548	Spencer *et al*., 2014[10]
425	Scheel *et al*., 2014[11]
340	Sinnecker *et al*., 2013[12]
340	Lee *et al*., 2012[13]
286	Lopez-Izquierdo *et al*., 2014[14]
414	Ma *et al*., 2011[15]
392	This study

2. Supplementary Methods

Flow cytometry

100 uL of 10^{11} PFU/ml of lentivirus containing either ASAP1 or GCaMP6f gene was added to a single well of a 24 well plate, with iPSC-CMs seeded at a density of 2.5 x10^5 cells/well. Flow cytometery was done 7-10 days after the addition of virus using an Accuri C6 flow cytometer (BD Biosciences).

Sequencing of CALM2 genomic DNA

Genomic DNA was isolated from iPSCs using DNeasy Blood & Tissue Kit (Qiagen) following manufacturer's protocol. A portion of *CALM2* 200 base pairs up and downstream from the c.389 A>G mutation was cloned using standard PCR (forward primer: 5'-AGGTGTCACTTGACTTTGGGA-3'; reverse primer: 5'-ATTTCAGGGGAAGGGTCACT-3') Standard Sanger sequencing was performed on the PCR product using the aforementioned forward primer.

Immunohistochemistry

Standard fluorescent immunohistochemistry was performed on non-differentiated iPSCs and embryoid bodies. Briefly, cells were fixed with 4% paraformaldehyde, permeabilized with 0.1% Triton X, and stained with primary, secondary antibodies, and finally counter-stained with DAPI for nuclear visualization. Primary antibodies included (manufacturer, catalog number): polyclonal rabbit anti-Oct4 IgG (AbCaM, ab19857), polyclonal rabbit anti-nanog IgG (AbCaM, ab80892), monoclonal mouse anti-SSEA4 IgG (AbCaM, ab16287), polyclonal rabbit anti-glial fibrillary acidic protein Ig (Dako, Z0334), rabbit polyclonal anti-smooth muscle action IgG (AbCaM, ab5694), and mouse monoclonal anti-α-fetoprotein IgG1 (R&D Systems, MAB1368). Secondary antibodies (all purchased from Invitrogen) include (catalog number): 594 goat anti-mouse IgG (A-11020), 594 donkey anti-rabbit IgG (A-21207), 488 goat anti-mouse IgG (A-31620), and 488 donkey anti-rabbit IgG (A-21206).

Embryoid body formation analysis

Embryoid bodies (EBs) were formed using a previously described method[16]. Briefly, iPSCs were enzymatically dissociated using Accutase (Sigma Aldrich) and transferred into low-attachment tissue culture plates filled with EB medium to allow clusters of cells grown in suspension. After 8 days, EBs were transferred onto gelatin-coated treated tissue culture plates. EBs were then collected for analysis after 25 days in culture. EB medium included 20% FBS in knockout DMEM (ThermoFisher Scientific, 10829018) supplemented with 1% L-glutamine, 1% non-essential amino acids, 1% penicillin-streptomycin, and 0.1 mmol/L β-mercapto ethanol.

Teratoma formation

Teratoma formation analysis was performed as previously described[17]. Briefly, 5x10^6 of undifferentiated iPSCs were mixed with Matrigel (BD Biosicences) at a 1:1 ratio and injected intramuscularly into NOD/SCID IL2 receptor gamma chain knockout (NSG) mice. Teratomas were harvested 5-8 weeks post injection, paraffin-embedded, sectioned, and stained with hematoxylin and eosin.

Western blot for CaM protein quantification

IPSC-CMs were collected 8-9 days post transduction. Cells were lyzed in a Tris-HCl based buffer and a western blot of the collected protein was performed as previously described[18]. All samples were run in duplicate on 12.5% Tris-HCl precast gels (Bio-Rad) in 25 mmol/L Tris, 192 mmol/L glycine, and 0.1% (wt/vol) SDS running buffer. Primary antibody incubations were performed overnight at 4°C using rabbit monoclonal anti-calmodulin antibody (Abcam, Cat. No. ab45689). Relative band densities were quantified using ImageJ software. The intensity of the bands was normalized by the total amount of protein obtained from a Coomassie stain.

SR content measurement

SR content was measured using the ratiometric calcium dye Indo-1 AM. Cells were loaded with 1μmol/L dye for 30 minutes at 37 °C, and rinsed 3 times, followed by an additional 10 minutes incubation in Tyrodes at 37 °C to allow for de-esterification of Indo-1 AM. Cells were stimulated for several minutes by application of an electric field across the coverslip using a C-Pace electrical stimulator (Ion Optix). The bath solution was then exchanged for a Na^+-free Tyrode's solution (Na^+ was replaced with choline ion to minimize the action of Na-Ca exchanger) with 1.8 mmol/L Ca^{2+}, and 10 mmol/L 2,3-butanedione monoxime. After baseline imaging, SR content was determined by the addition of 5 mmol/L caffeine. Fluorescence was measured using 340-nm excitation and 405- and 485-nm emission wavelengths. The intracellular Ca^{2+} concentration ($[Ca^{2+}]$) was calculated as $[Ca^{2+}] = K_{d/Indo} \cdot \beta \cdot (R - R_{\min})/(R_{\max} - R)$, where R is the ratio of fluorescence signal at 405 and 485 nm. $K_{d/Indo}$ was 800 nmol/L[8]. $R_{\min}$ was determined to be 0.33 in a ~ 0 mmol/L Ca^{2+} Tyrode's after 30 min incubation with BAPTA-AM. $R_{\max}$ was determined to be 20.85 in a Na^+-free Tyrode's (Na^+ was replaced with choline ion to minimize the action of Na-Ca exchanger) with 10 mmol/L Ca^{2+}, 25 μmol/L digitonin and 10 mmol/L 2,3-butanedione monoxime. β, as defined by the ratio of fluorescence signal at 485 nM under Ca^{2+}-free and Ca^{2+}-bound conditions, was determined to be 0.85.

Ventricular myocyte model (LRd model)

The original LRd model[2] was adjusted as previously described such that the duration and shape of the action potential was more similar to human[1]. Additional adjustments were made to the LTCC module, primarily substituting a CDI specific deficit expected for calmodulinopathy into a variable fraction of LTCC channels. Equations governing the final LTCC channel pools are as follows:

For the CDI gate (f_{CDI}):

$$k_{on} = 4 \cdot 10^3 \quad \text{mM}^{-2}\text{ms}^{-1} \tag{1}$$

$$k_{off} = 1 \cdot (K_{CDI})^2 \cdot k_{on} \quad \text{ms}^{-1} \tag{2}$$

$$df_{CDI} = k_{on} \cdot [Ca]^2 \cdot f_{CDI} + k_{off} \cdot (1 - f_{CDI}) \tag{3}$$

$$K_{CDI} = 6.325\text{e}^{-4} \quad \text{mM}$$

(4)

The activation gate (d), followed standard Hodgkin and Huxley equations[19]:

$$dd = \frac{d_{steadystate} - d}{\tau_d} \tag{5}$$

$$d^1_{steadystate} = \frac{1}{1 + e^{-(V+14)/(25/2)}} \tag{6}$$

$$d^2_{steadystate} = \frac{1}{1 + e^{-(V+14-15)/(25/1.5)}} \tag{7}$$

$$d_{steadystate} = d^1_{steadystate} \cdot d^2_{steadystate} \tag{8}$$

$$\tau_d = 0.59 + \frac{5}{1 + e^{-3 \cdot 0.052(V+20)+15}} \cdot \frac{1}{1 + e^{2 \cdot 0.052(V+20)-75}} \tag{9}$$

The voltage dependent inactivation gate (f):

$$df = \frac{f_{steadystate} - f}{\tau_f} \tag{10}$$

$$f_{steadystate} = 1 - 0.4 \cdot (1 - \frac{1}{1 + e^{(V+32)/8}} \cdot \frac{0.8}{1 + e^{(50-V)/20}}) \tag{11}$$

$$\tau_f = \frac{30}{0.0197 \cdot e^{-0.0337(V+10)^2 + .02}} \tag{12}$$

With the gates set, the total current through the L-type channel, as well as the Na^+/Ca^{2+} exchange current and Ca^{2+} activated potassium channel was defined as:

$$i_{Ca,Ltype} = d \cdot f \cdot (f_{CDI} + P_O^{modeCa}(1 - f_{CDI})) \cdot i_{Ca} \tag{13}$$

$$i_{Na/Ca} = d \cdot f \cdot (f_{CDI} + P_O^{modeCa}(1 - f_{CDI})) \cdot i_{Na} \tag{14}$$

$$i_{K_{Ca}} = d \cdot f \cdot (f_{CDI} + P_O^{modeCa}(1 - f_{CDI})) \cdot i_K \tag{15}$$

$$P_O^{modeCa} \text{ xviii } 0.1$$

(16)

Where P_O^{modeCa} represents the relative open probability of the L-type channel in mode Ca^{2+} as compared to mode 1. i_{Ca}, i_{Na} and i_K represent the single channel open level as set by the GHK equation.

With the wild type channel in place, a second pool of LTCC channels were added to simulate the effect of CaM_{D130G} on the channel. Properties of this pool of channels were made based on this study and on the previous biophysical characterization of these channels[8]. This pool of channels was modeled as above, except for the following alterations:

$$k_{on} = 1000 * 4 \cdot 10^3 \quad \text{mM}^{-2}\text{ms}^{-1} \tag{17}$$

$$k_{off} = 10^{-3} \cdot (K_{CDI})^2 \cdot k_{on} \quad \text{ms}^{-1} \tag{18}$$

$$df_{CDI} = k_{on} \cdot [Ca]^2 \cdot f_{CDI} + k_{off} \cdot (1 - f_{CDI}) \tag{19}$$

$$P_O^{D130G,modeCa} = 0.95 \tag{20}$$

All other equations in the model not mentioned here were identical to those described[1] and are entirely based on the original 2007 LRd model[2].

3. Supplementary References

1. Dick IE, Joshi-Mukherjee R, Yang W, Yue DT. Arrhythmogenesis in timothy syndrome is associated with defects in ca(2+)-dependent inactivation. *Nat Commun*. 2016;7:10370
2. Livshitz LM, Rudy Y. Regulation of ca2+ and electrical alternans in cardiac myocytes: Role of camkii and repolarizing currents. *Am. J. Physiol. Heart Circ. Physiol.* 2007;292:H2854-2866
3. Luo CH, Rudy Y. A dynamic model of the cardiac ventricular action potential. I. Simulations of ionic currents and concentration changes. *Circ. Res.* 1994;74:1071-1096
4. Luo CH, Rudy Y. A dynamic model of the cardiac ventricular action potential. Ii. Afterdepolarizations, triggered activity, and potentiation. *Circ. Res.* 1994;74:1097-1113
5. Petryszak R, Burdett T, Fiorelli B, Fonseca NA, Gonzalez-Porta M, Hastings E, Huber W, Jupp S, Keays M, Kryvych N, McMurry J, Marioni JC, Malone J, Megy K, Rustici G, Tang AY, Taubert J, Williams E, Mannion O, Parkinson HE, Brazma A. Expression atlas update--a database of gene and transcript expression from microarray- and sequencing-based functional genomics experiments. *Nucleic Acids Res.* 2014;42:D926-932
6. Kane C, Couch L, Terracciano CM. Excitation-contraction coupling of human induced pluripotent stem cell-derived cardiomyocytes. *Front Cell Dev Biol*. 2015;3:59
7. Rocchetti M, Sala L, Dreizehnter L, Mura M, Altomare C, Bernardi J, Ronchi C, Severi S, George AL, Schwartz PJ, Sinnecker D, Gnecchi M, Crotti L, Moretti A, Zaza A. Human induced pluripotent stem cells-derived cardiomyocytes carrying calm1-f142l mutation recapitulate lqts phenotype in vitro. *Biophysical Journal*.110:263a
8. Limpitikul WB, Dick IE, Joshi-Mukherjee R, Overgaard MT, George AL, Jr., Yue DT. Calmodulin mutations associated with long qt syndrome prevent inactivation of cardiac l-type ca(2+) currents and promote proarrhythmic behavior in ventricular myocytes. *J. Mol. Cell. Cardiol.* 2014;74:115-124
9. Du DT, Hellen N, Kane C, Terracciano CM. Action potential morphology of human induced pluripotent stem cell-derived cardiomyocytes does not predict cardiac chamber specificity and is dependent on cell density. *Biophys. J.* 2015;108:1-4
10. Spencer CI, Baba S, Nakamura K, Hua EA, Sears MA, Fu CC, Zhang J, Balijepalli S, Tomoda K, Hayashi Y, Lizarraga P, Wojciak J, Scheinman MM, Aalto-Setala K, Makielski JC, January CT, Healy KE, Kamp TJ, Yamanaka S, Conklin BR. Calcium transients closely reflect prolonged action potentials in ipsc models of inherited cardiac arrhythmia. *Stem Cell Reports*. 2014;3:269-281
11. Scheel O, Frech S, Amuzescu B, Eisfeld J, Lin KH, Knott T. Action potential characterization of human induced pluripotent stem cell-derived cardiomyocytes using automated patch-clamp technology. *Assay Drug Dev Technol*. 2014;12:457-469
12. Sinnecker D, Goedel A, Dorn T, Dirschinger RJ, Moretti A, Laugwitz KL. Modeling long-qt syndromes with ips cells. *J. Cardiovasc. Transl. Res.* 2013;6:31-36
13. Lee P, Klos M, Bollensdorff C, Hou L, Ewart P, Kamp TJ, Zhang J, Bizy A, Guerrero-Serna G, Kohl P, Jalife J, Herron TJ. Simultaneous voltage and calcium mapping of genetically purified human induced pluripotent stem cell-derived cardiac myocyte monolayers. *Circ. Res.* 2012;110:1556-1563
14. Lopez-Izquierdo A, Warren M, Riedel M, Cho S, Lai S, Lux RL, Spitzer KW, Benjamin IJ, Tristani-Firouzi M, Jou CJ. A near-infrared fluorescent voltage-sensitive dye allows for moderate-throughput electrophysiological analyses of human induced pluripotent

stem cell-derived cardiomyocytes. *Am. J. Physiol. Heart Circ. Physiol.* 2014;307:H1370-1377

15. Ma J, Guo L, Fiene SJ, Anson BD, Thomson JA, Kamp TJ, Kolaja KL, Swanson BJ, January CT. High purity human-induced pluripotent stem cell-derived cardiomyocytes: Electrophysiological properties of action potentials and ionic currents. *Am. J. Physiol. Heart Circ. Physiol.* 2011;301:H2006-2017
16. Limphong P, Zhang H, Christians E, Liu Q, Riedel M, Ivey K, Cheng P, Mitzelfelt K, Taylor G, Winge D, Srivastava D, Benjamin I. Modeling human protein aggregation cardiomyopathy using murine induced pluripotent stem cells. *Stem Cells Transl Med*. 2013;2:161-166
17. Ye Z, Liu CF, Lanikova L, Dowey SN, He C, Huang X, Brodsky RA, Spivak JL, Prchal JT, Cheng L. Differential sensitivity to jak inhibitory drugs by isogenic human erythroblasts and hematopoietic progenitors generated from patient-specific induced pluripotent stem cells. *Stem Cells*. 2014;32:269-278
18. O'Rourke B, Kass DA, Tomaselli GF, Kaab S, Tunin R, Marban E. Mechanisms of altered excitation-contraction coupling in canine tachycardia-induced heart failure, i: Experimental studies. *Circulation research*. 1999;84:562-570
19. Hodgkin AL, Huxley AF. A quantitative description of membrane current and its application to conduction and excitation in nerve. *The Journal of physiology*. 1952;117:500-544